Metsähovi Publications on Radio Science
Espoo 2002 HUT-MET-42

VLBI and total flux density investigations of the structure of active galactic nuclei

Kaj Wiik

Dissertation for the degree of Doctor of Technology to be presented with due permission for public examination and debate in Auditorium S4 at Helsinki University of Technology (Espoo, Finland) on the 15$^{\mathrm{th}}$ of November, 2002, at 12 o'clock noon.

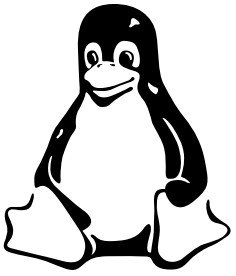

"[Linux] does endless loops in six seconds."
–Linus Torvalds

Abstract

This doctoral thesis studies the structure of active galactic nuclei (AGN) using very long baseline interferometry (VLBI) at high radio frequencies (22 – 86 GHz). The VLBI observations are complemented using information from total flux density (TFD) observations at the corresponding frequencies and the TFD variations are compared to the structure changes seen in the VLBI images.

The basis of this work is the data from the three epoch VLBI monitoring project, which produced 45 images and parameters of 15 extragalactic sources at 22 GHz.

The maximum intrinsic brightness temperature for synchrotron sources is assumed to be limited by the inverse Compton catastrophe to $\simeq 10^{12}$ K. We have presented two new methods to estimate this limit using total flux density observations, synchrotron-Self-Compton X-ray fluxes and shock parameters from VLBI observations. Using several data sets, we find that both methods yield a value of $\leq 10^{11}$ K, which is consistent with the equipartition limit of $10^{10} - 10^{11}$ K.

We have developed a new method for estimating the geometry of the Universe using the linear sizes of shocks in AGN jets. The angular sizes of the shocks from VLBI observations are normalized using intrinsic diameter estimates from TFD observations. Using a very small set of test data, we verify that the accuracy of the derived values compare favourably with traditional methods using much larger samples.

A clear connection between radio and gamma-ray flares and VLBI component ejections was found. Furthermore, it was shown that the origin of the gamma-ray flares is in the shocks and that they can not be produced close to the core of the AGN.

A helical structure was found in the jet of CTA 102, a High Polarised Quasar (HPQ). The apparent proper motions in the jet varied from 4.2 to 13.8 times the speed of the light. This work combined the work of several years of observation, covering wavelengths from 1.3 to 12 mm and angular resolutions from 50 to 500 microarcseconds.

The first 2mm VLBI experiment between Pico Veleta and Metsähovi was performed and correlation fringes were detected on a baseline of 1.55 billion wavelengths. The success of this experiment shows that VLBI observations are possible at very high frequencies leading to very high resolution and enabling to produce images of the fine structure of the cores of the AGN.

Acknowledgements

This research was carried out both at the Tuorla Observatory and the Metsähovi Radio Observatory. I am deeply indebted to Profs. Seppo Urpo (Metsähovi), Mauri Valtonen (Tuorla) and Esko Valtaoja (Tuorla/Metsähovi) for giving me the opportunity to write this thesis. Prof. Esko Valtaoja has been remarkably patient as my supervisor, giving enough 'leash' and tightened it at times to get papers published in finite amount of time.
The unique atmosphere and the people at Tuorla have encouraged me and have given an opportunity to discuss any aspect of astronomy, and also life, as we know it... Especially the people at the (former) 'rivitalo': Jyrki Hänninen, Pasi Hakala, Seppo Wirén, and others, it has been very interesting to work with you!
Tuomas Savolainen has been the nearest co-author during the last years, always full of new ideas and ready for discussions, cheers!
I wish to thank the nice people at Metsähovi, especially the ultra-sturdy VLBI gang, both past and present, now co-ordinated by Prisse Könönen, who have kept the tapes (soon disks!) running often in impossible conditions.
Also the best A(GN)-group, namely Merja Tornikoski, Anne Lähteenmäki and the disciples, thanks for enjoyable collaboration!
Kari Leppänen, you introduced me to the chilling intricacies of VLBI data reduction in the heat of Socorro, cheers!
Many thanks to my parents for the care and support!
And finally, I admire the patience that Silja and Mörri, my closest companions, have shown in the last few years. Thank you for your love and support (and interesting discussions, with Silja I mean..).
This work has been financially supported by the Academy of Finland, especially the Finnish Graduate School in Astronomy and Space Physics, and Vilho, Yrjö and Kalle Väisälä foundation, and Emil Aaltonen foundation.

Tuorla, October 2002

Kaj Wiik

Contents

1 Introduction **1**

2 VLBI **2**
2.1 Basic theory 2
2.2 Imaging 8
2.3 High resolution VLBI 12

3 Active Galactic Nuclei **16**
3.1 Basic Model 16
3.2 Jets 16

4 Total flux density variations and VLBI **19**
4.1 Decompositions of total flux density time series 19
4.2 Relativistic effects 20
4.3 Connections between radio flares and VLBI images 22
4.4 Curvature of the jet and stationary features 26
4.5 VLBI and cosmology 29

5 Discussion of the papers **32**
5.1 Three epoch survey of 15 AGN at 22 GHz 32
5.2 Comparison of VLBI and TFD data: new methods determining limiting brightness temperature $T_{\mathrm{b,lim}}$ and Doppler factor. 32
5.3 VLBI and cosmology 32
5.4 Structure of the core region and the jet 33
5.5 2mm VLBI 33

List of publications

This thesis consists of an introduction and the following ten publications:

[P1] Lähteenmäki, A., Valtaoja, E., Wiik, K., 1999, "Total flux density variations in extragalactic radio sources. II. Determining the limiting brightness temperature for synchrotron sources", The Astrophysical Journal, 511, 112.

[P2] Wiik, K., Valtaoja, E., 2001, "The geometry of the universe from high resolution VLBI data of AGN shocks", Astronomy & Astrophysics, 366, 1061.

[P3] Wiik, K., Valtaoja, E., Leppänen, K., 2001, "VLBI monitoring of a sample of 15 AGN at 22 GHz. I. Data", Astronomy & Astrophysics, 380, 72.

[P4] Valtaoja, E., Savolainen, T., Wiik, K., Lähteenmäki, A., 2002, "Millimetre Continuum Variations, VLBI Structure, and Gamma-rays: Investigating Shocked Jet Physics", Publications of the Astronomical Society of Australia, 19, 117.

[P5] Greve, A., Könönen, P., Graham, D. A., Wiik, K., Krichbaum, T. P., Conway, J., Rantakyrö, F., Urpo, S., Grewing, M., Booth, R. S., John, D., Navarro, S., Mujunen, A., Ritakari, J., Peltonen, J., Sjöman, P., Berton, M., 2002, "147 GHz VLBI Observations: Detection of 3C 273 and 3C 279 on the 3 100 km Baseline Metsähovi – Pico Veleta", Astronomy & Astrophysics, 390, L19.

[P6] Savolainen, T., Wiik, K., Valtaoja, E., Jorstad, S. G., Marscher, A. P., 2002, "Connections Between Millimeter Continuum Variations and VLBI Structure in 27 AGN", Astronomy & Astrophysics (in press).

[P7] Rantakyrö, F. T., Wiik, K., Tornikoski, M., Valtaoja, E., Bååth, L. B., 2002, "Multifrequency Interferometer and Radio Continuum Monitoring Observations of CTA 102", Helsinki University of Technology, Metsähovi Publications on Radio Science HUT-MET-37; submitted to Astronomy & Astrophysics.

[P8] Wiik, K., Valtaoja, E., Lähteenmäki, A., 2000, "Comparison of Total Flux and VLBI Properties of a Sample of Fifteen AGN at 22 GHz", in Astrophysical Phenomena Revealed by Space VLBI, Proceedings of the VSOP Symposium Eds.: H. Hirabayashi, P.G. Edwards, and D.W. Murphy, Published by the Institute of Space and Astronautical Science, Kanagawa, Japan, 321.

[P9] Valtaoja E, Wiik K, 1999, “AGN shocks as cosmological standard rods”, Second Millimeter-VLBI Science Workshop, IRAM Granada, Spain, 21.

[P10] Wiik, K., Valtaoja, E., 1998, “Comparison of Total Flux and VLBI Properties of a Sample of 15 AGN at 22 GHz”, ASP Conference Series, 1998, Volume 144, IAU Colloquium 164, eds. J.A. Zensus, G.B. Taylor, & J.M. Wrobel, 144, 151.

In paper [P1] I was responsible for the reduction of our own VLBI data used in the paper and for the relevant data analysis. For paper [P2] I performed the data reduction, wrote computer programs for the model fitting and was responsible for writing the paper. In paper [P3] I was responsible for the VLBI data reduction and also for the scheduling the third observation epoch. I also wrote a computer program to plot the data and had the sole responsibility for writing the paper. Paper [P4] used the VLBI data obtained in my programs. I also wrote the VLBI-related part of the paper, and participated in the general data analysis. For paper [P5] I was responsible for starting the project with the P.I. and for conducting preliminary feasibility discussions, and consulted in setting up the experiment in Finland. I also designed the quasioptics for the receiver setup. In paper [P6] I was responsible for rereducing the VLBI data and writing and modifying computer programs to enable the detailed analysis of the closure phase data, a central argument of the paper. I also wrote the relevant parts of the paper. For paper [P7] I performed the data reduction and more detailed analysis for most (4/5 epochs) of the 22 GHz and all 43 GHz data and I also scheduled the simultaneous 22/43 VLBI observation, and participated in the writing of the paper. Additionally, for papers [P1], [P2], [P3], [P4], [P6], and [P7] I participated in discussions about the quality and reliability of the VLBI data. I had the sole responsibility for writing the papers [P8] and [P10] and participated in the writing of the paper [P9].

CHAPTER 1
Introduction

The ideal object to be studied using very long baseline interferometry (VLBI) is bright, far away and has a small angular size. Active galactic nuclei (AGN) fulfil all these criteria and therefore form a perfect match with VLBI.

Active galaxies form an interesting subgroup that can be characterised by variability and luminosity. They produce a luminosity of thousand 'normal' galaxies in a volume of space less than the distance to the nearest star. The luminosity is also variable, timescales of days to years are most common. This work focuses mainly in studying the emission in radio frequencies, dictated by the limitations of current state of the art VLBI.

Because observing time in VLBI is a very limited resource, it is not usually possible to observe frequently enough compared with the structure changes in the source. Therefore it is sometimes very difficult to identify the moving shocks between the observation epochs. Therefore, single dish total flux density (TFD) monitoring data is a valuable resource not only for identifying the components but also providing a means to derive key parameters that characterise the emitting region.

The radio emission from AGN is coming from a relativistic jet that is aimed closely to the line of sight. The viewing angle and the velocity of the shocks in the jet are the main parameters that define the magnitude of the relativistic effects that are observed in the source. The Doppler factor combines conveniently these parameters and describes the enhancement of emission due to the relativistic effects. If the relativistic effects can be estimated, the intrinsic properties of the shock and jet can be calculated.

As an example, one fundamental parameter of synchrotron emission is the maximum intrinsic brightness temperature. It is usually assumed to be $\simeq 10^{12}$ K, due to an effect called the inverse Compton catastrophe, but our results show that an alternative upper value of $\simeq 10^{11}$ is more plausible. This leads to a different limiting mechanism, the equipartition of energy between the radiating particles and the magnetic field.

Formerly the total sizes of radio sources or the shock to core separations have been used to probe the geometry of the Universe but unfortunately they suffer from biases and evolutionary effects and therefore at least a very large number of observations are needed to get useful results. In this work, the normalized sizes of the individual shocks are proposed to be used instead for this purpose. The linear size of the shock is estimated from TFD monitoring using the light travel time arguments and the angular size estimate is obtained using VLBI. This normalized size, measured in milliarcseconds/lightday, traces the geometry of the universe as it is observed at different distances.

CHAPTER 2
VLBI

2.1 Basic theory

This introduction of the main principles of interferometry follows closely the clear and beautiful treatment by Clark (1998).

2.1.1 Observed electric field

Consider a source emitting a quasi-monochromatic (narrow bandwidth) electric field $\boldsymbol{E}_\nu(\boldsymbol{R})$ at $\boldsymbol{R}$. To avoid tensor quantities and to keep the equations easily understandable, let us forget the polarisation properties of the field and treat $\boldsymbol{E}_\nu(\boldsymbol{R})$ as a scalar field $E_\nu(\boldsymbol{R})$.
For simplicity, the distance $\boldsymbol{R}$ to the emitting source will be considered as very large, $|\boldsymbol{R}| \gg B^2/\lambda$, where B is the baseline length. Therefore, we can only observe the surface brightness on an imaginary sphere with a radius of $\boldsymbol{R}$, all information on depth is lost. Because no radiation is emitted inside the sphere, Huygens' principle can be used to express the field of the source using the propagated electric field on the surface of the sphere,

$$E_\nu(\boldsymbol{r}) = \int \mathcal{E}_\nu(\boldsymbol{R}) \frac{e^{2\pi i\nu|\boldsymbol{R}-\boldsymbol{r}|/c}}{|\boldsymbol{R}-\boldsymbol{r}|} \mathrm{d}S, \tag{2.1}$$

where $\mathrm{d}S$ is a surface area element on the sphere.

2.1.2 Spatial coherence function

A correlation between two points $\boldsymbol{r}_1$ and $\boldsymbol{r}_2$ of the field or the spatial coherence function can be defined as the expectation of the complex conjugate product of the fields:

$$\vee_\nu(\boldsymbol{r}_1, \boldsymbol{r}_2) = \langle \boldsymbol{E}_\nu(\boldsymbol{r}_1) \boldsymbol{E}^*_\nu(\boldsymbol{r}_2) \rangle. \tag{2.2}$$

Using Eq. 2.1, we get

$$\vee_\nu(\boldsymbol{r}_1, \boldsymbol{r}_2) = \left\langle \iint \mathcal{E}_\nu(\boldsymbol{R}_1) \mathcal{E}^*_\nu(\boldsymbol{R}_2) \frac{e^{2\pi i\nu|\boldsymbol{R}_1-\boldsymbol{r}_1|/c}}{|\boldsymbol{R}_1-\boldsymbol{r}_1|} \frac{e^{2\pi i\nu|\boldsymbol{R}_2-\boldsymbol{r}_2|/c}}{|\boldsymbol{R}_2-\boldsymbol{r}_2|} \,\mathrm{d}S_1 \,\mathrm{d}S_2 \right\rangle. \tag{2.3}$$

Because the radiation from any (natural) astronomical object is not spatially coherent or $\langle \mathcal{E}_\nu(\boldsymbol{R}_1) \mathcal{E}^*_\nu(\boldsymbol{R}_2) \rangle \equiv 0$, when $\boldsymbol{R}_1 \neq \boldsymbol{R}_2$, we can simplify further:

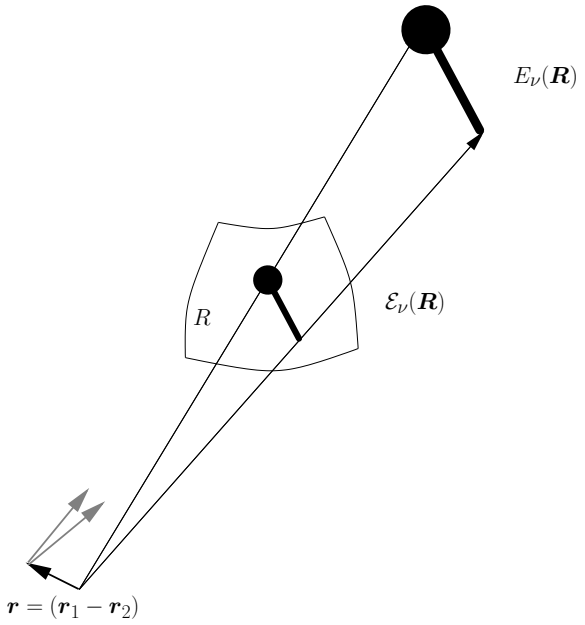

Figure 2.1: If the distance to the emitting source is very large when compared to the baseline length, we can assume that all radiation is coming from a far-away imaginary sphere with a radius R, and by further neglecting small terms the spatial coherence function becomes dependent only on the baseline difference vector $r = (r_1 - r_2)$.

$$\vee_\nu(\boldsymbol{r}_1, \boldsymbol{r}_2) = \int \langle |\mathcal{E}_\nu(\boldsymbol{R})|^2 \rangle |\boldsymbol{R}|^2 \frac{e^{2\pi i \nu |\boldsymbol{R}-\boldsymbol{r}_1|/c}}{|\boldsymbol{R}-\boldsymbol{r}_1|} \frac{e^{2\pi i \nu |\boldsymbol{R}-\boldsymbol{r}_2|/c}}{|\boldsymbol{R}-\boldsymbol{r}_2|} \, \mathrm{d}S. \tag{2.4}$$

2.1.3 Intensity of the electric field

The observed intensity produced by the electric field on the surface of the imaginary sphere $\mathcal{E}_\nu(\boldsymbol{R})$ is

$$I_\nu(\boldsymbol{s}) = |\boldsymbol{R}|^2 \langle |\mathcal{E}_\nu(\boldsymbol{s})|^2 \rangle, \tag{2.5}$$

where $\boldsymbol{s}$ is the unit vector $\boldsymbol{R}/|\boldsymbol{R}|$.
When we assume (again) that the distance to the source and the imaginary sphere is large, we can neglect small terms and replace the surface element $\mathrm{d}S$ by $|\boldsymbol{R}|^2 \, \mathrm{d}\Omega$, we get:

$$\vee_\nu(\boldsymbol{r}_1, \boldsymbol{r}_2) \approx \int I_\nu(\boldsymbol{s}) e^{2\pi i \nu \, \boldsymbol{s}\cdot(\boldsymbol{r}_1 - \boldsymbol{r}_2)/c} \, \mathrm{d}\Omega. \tag{2.6}$$

This function is the *spatial autocorrelation function* and it depends only on the separation vector $\boldsymbol{r}_1$- $\boldsymbol{r}_2$ of the observing points. The function can be measured simply by varying the baseline and holding one observation point fixed, observations from all possible pairs are not required.

2.1.4 Observations in the UV-plane

Finally, we can decide that all observations will be performed in a plane that is perpendicular to $\boldsymbol{s}$. Furthermore we can choose a coordinate system where the separation vector is measured in wavelengths $\boldsymbol{r}_1 - \boldsymbol{r}_2 = \lambda(u, v, 0)$ and the components of the unit vector $\boldsymbol{s}$ are $(l, m, \sqrt{1 - l^2 - m^2})$. In this coordinate system the spatial autocorrelation function (Eq. 2.6) can be expressed as

$$\vee_\nu(u, v, w \equiv 0) = \iint I_\nu(l, m) \frac{e^{-2\pi i(ul+vm)}}{\sqrt{1 - l^2 - m^2}} \, \mathrm{d}l \, \mathrm{d}m. \tag{2.7}$$

This equation is a Fourier transform relation between $\vee_\nu(u, v, w \equiv 0)$ and the modified intensity $I_\nu(l, m)/\sqrt{1 - l^2 - m^2}$, where the angles are expressed as direction cosines. Before we can go ahead and try to invert this equation, i.e., start imaging, two deviations from the ideal case must be discussed.

2.1.5 Discrete sampling of $\vee_\nu(u, v)$ with finite sized antennas

We can measure the spatial autocorrelation function only in a finite amount of discrete points that can be described by a sampling function $S(u, v)$. This sampling function produces the *synthesised* or *dirty beam*, which is better known as the *point spread function* (PSF) in the optical community:

$$B(l, m) = \iint S(u, v) \, e^{2\pi i(ul+vm)} \, \mathrm{d}u \, \mathrm{d}v. \tag{2.8}$$

In practice dirty beam will be further modified by time varying amplitude and phase or *complex gain* of the observing antennas.
What is really observed is the *dirty image* I_ν^D that is the convolution of the true intensity and the dirty beam:

$$I_\nu^D(l, m) = \iint \vee_\nu(u, v) S(u, v) e^{2\pi i(ul+vm)} \, \mathrm{d}u \, \mathrm{d}v = I_\nu * B. \tag{2.9}$$

Performing the corresponding deconvolution is the most difficult problem in VLBI and it will be discussed further in Section 2.2.2.
The dirty image will be multiplied with the *primary beam* $\mathcal{A}_\nu(l, m)$ of the finite sized receiving antennas:

$$V_\nu(u,v) = \iint \mathcal{A}_\nu(l,m)\, I^D_\nu(l,m)\, e^{-2\pi i(ul+vm)}\, \mathrm{d}l\, \mathrm{d}m. \tag{2.10}$$

$V_\nu(u,v)$ is finally the observed *complex visibility*.

2.1.6 Atmosphere

The atmosphere affects both the amplitude and the phase of the received signal. The resonance lines of oxygen (60 and 118 GHz) and water vapour (22 and 183 GHz) are responsible for most of the absorption or the *opacity*, τ of the atmosphere.
The noise temperature that is detected by the receiver through the atmosphere, or the *system noise temperature* ($T_{\rm sys}$), is the sum of the attenuated signal from the source ($T_{\rm src}$), noise emitted by the atmosphere, spillover radiation from the ground ($T_{\rm spill}$), and noise generated in the receiving equipment ($T_{\rm rec}$):

$$T_{\rm sys} = T_{\rm src}e^{-\tau} + T_{\rm atm}(1-e^{-\tau}) + T_{\rm rec} + T_{\rm spill}, \tag{2.11}$$

where $T_{\rm atm}$ is the average temperature along the line of sight, or the *effective physical temperature of the atmosphere*. $T_{\rm atm}$ can be approximated, e.g., by the following experimental relation, which is valid in the frequency range of 20 – 100 GHz (Leppänen 1993 and references therein):

$$T_{\rm atm} = 0.652 \cdot \max\{T_{\rm ground}\} + 84.6{\rm K}. \tag{2.12}$$

Here $\max\{T_{\rm ground}\}$ is the maximum ground level temperature of the day.
The system noise temperature can be scaled to the top of the atmosphere:

$$T_{\rm eff} = e^{\tau}[T_{\rm atm}(1-e^{-\tau}) + T_{\rm rec} + T_{\rm spill}] + T_{\rm src}, \tag{2.13}$$

$T_{\rm eff}$ is called as the *effective system noise temperature*.
Atmospheric opacity can be determined from *sky dip observations* where $T_{\rm sys}$ is measured at different elevation angles. $T_{\rm sys}$ depends on the zenith opacity (τ_0) and the zenith angle as follows:

$$T_{\rm sys} = T_{\rm atm}(1-e^{-\tau_0 \sec(z)}) + T_{\rm rec} + T_{\rm spill}(z). \tag{2.14}$$

τ_0 can now be obtained by fitting function 2.14 to the measurements.
If accurate receiver noise temperature (and the contribution of spillover radiation) is known, the atmospheric attenuation $L = e^{\tau}$ along the line of sight can be calculated simply from the *sky noise temperature* $T_{\rm sky}$

$$T_{\rm sky} = T_{\rm atm}(1-e^{-\tau}) = T_{\rm sys} - T_{\rm src} - T_{\rm rec} - T_{\rm spill}(z), \tag{2.15}$$

and $T_{\rm atm}$ by

$$L = \frac{T_{\rm atm}}{T_{\rm atm} - T_{\rm sky}}. \tag{2.16}$$

In addition to variations in attenuation, the changes in the refractive index of atmosphere cause variations also in the path length and therefore lead to phase noise. The refractive index n determines the phase shift experienced of a wave travelling a distance D through the medium (Carilli et al. 1998):

$$\phi = \frac{2\pi}{\lambda} \cdot n \cdot D. \tag{2.17}$$

For convenience the refraction index is typically given with respect to vacuum $N = (n-1) \times 10^6$ and can be divided into dry and wet (water vapour) components:

$$N_{\rm d} = 2.2 \cdot 10^5 \cdot \rho_{\rm tot} \tag{2.18}$$

$$N_{\rm wv} = 1.7 \cdot 10^9 \cdot \frac{\rho_{\rm wv}}{T_{\rm atm}}, \tag{2.19}$$

where $\rho_{\rm tot}$ and $\rho_{\rm wv}$ are the total and the water vapour densities [g/cm^{-3}]. For our purposes the dry component can be considered as stable and the interest concentrates in the *precipitable water vapour column* $w = \rho_{\rm wv} \cdot D$. The electrical path length ($L_{\rm e}$) fluctuates due to variations in w (in normal conditions, $T_{\rm atm} \simeq 270$K):

$$L_{\rm e} = 1.7 \times 10^3 \frac{w}{T_{\rm atm}} \simeq 6.3 \times w. \tag{2.20}$$

The variations can be finally expressed in terms of phase:

$$\phi \simeq \frac{12.6\,\pi}{\lambda} \cdot w. \tag{2.21}$$

This relation is verified experimentally for a range of atmospheric conditions by Hogg et al. (1981).

Tropospheric phase noise can be reduced by *self calibration* (see section 2.2) where the observed source is used as a phase calibrator. This method can be used if the source is so strong that it can be detected in an integration time that is shorter than the timescale of the phase variations. *Phase referencing* can be used if a reasonably compact strong source can be found near the source to be observed. The array is switching between these sources and selfcalibration methods are applied to the reference source in order to correct the phase variations. After this, a longer integration time can be used for both of the sources and the weaker program source can be processed normally.

Another method that can be used in tracking the tropospheric delay variations is to try to estimate w from $T_{\rm sky}$. The fluctuating component of $T_{\rm sky}$ can be approximated by

$$T_{\rm sky}^{\rm rms} \simeq T_{\rm atm}\, e^{-\tau}\, [A_\nu w_{\rm rms} + \frac{(A_\nu w_{\rm rms})^2}{2}], \tag{2.22}$$

where A_ν is a scale factor that depends on frequency and current conditions (optical depth per millimetre of precipitable water vapour as a function of frequency, see Carilli et al. (1998) for details).

Eq. 2.22 can be inverted and so $T_{\rm sky}$ can be converted to phase change using Eq. 2.21. A_ν can be obtained from tropospheric parameters using an atmospheric model or empirically by observing a calibration source and fitting Eq. 2.22 to $T_{\rm sky}$ and the observed phase changes.

2.1.7 Antennas

The efficiency of a radio telescope can be expressed by the ratio K/Jy

$$\frac{T_{\rm src}}{S} = \frac{A_{\rm eff}}{2k} \cdot 10^{-26} \left[\frac{\rm K}{\rm Jy}\right], \tag{2.23}$$

which is often called the DPFU (degrees per flux unit) value of the antenna. In Eq. 2.23 k is the Boltzmann constant and $A_{\rm eff}$ is the antenna effective aperture [m^2] (Napier 1998):

$$A_{\rm eff} = A_{\rm phys} \cdot \eta_{\rm sf}\, \eta_{\rm bl}\, \eta_{\rm sp}\, \eta_{\rm il}\, \eta_{\rm rest}, \tag{2.24}$$

where $A_{\rm phys}$ is the physical aperture of the antenna and $\eta_{\rm sf}, \eta_{\rm bl}, \eta_{\rm sp}, \eta_{\rm il}$ are the efficiencies due to the surface accuracy, blockage, spillover and illumination efficiency respectively. The $\eta_{\rm rest}$ includes all other deficiencies, including the loss from pointing errors. This source of error can be considerable in VLBI because for most of the small antennas the sources are not detectable in total power mode and consequently can not be used for pointing corrections during the observations.
As a result the antenna pointing must be corrected using a *pointing function* that depends on current azimuth and elevation and possibly also the ambient temperature and humidity. The function is determined before the observing session by measuring the position errors using a number of strong sources, typically molecular masers and AGN's.

2.1.8 Receivers

The main parameters defining the performance of high frequency VLBI receivers are obviously receiver noise temperature $T_{\rm rec}$ and local oscillator stability.
Below 115 GHz, state of the art receivers utilise cryogenic high electron mobility transistor (HEMT) amplifiers with planar Schottky mixers at ambient temperature. Above 115 GHz active amplification is not (yet) practical and superconducting-insulator-superconductor (SIS) mixers with very low mixing loss are generally used.
Instead of conversion loss, SIS-mixers have gain around 1 and consequently the noise temperature requirement for the first intermediate frequency (IF) amplifier is relaxed.
The system noise temperature limit for phase conserving mixers and amplifiers can be set using quantum mechanics and the Heisenberg uncertainty principle (Thompson et al. 1986):

$$T^{\rm Q}_{\rm sys} \geq \frac{h\nu}{k}. \tag{2.25}$$

For example at 22 GHz $T^{\rm Q}_{\rm sys}$ is 1 K and at 150 GHz 7 K.
Because the phase reference (almost always a hydrogen maser) is multiplied either using real multiplication and mixing or phase-locked loops to the final frequency, all phase fluctuations are multiplied as well. This leads to high temperature and mechanical stability requirements for the local oscillator system. Also any risk of amplitude to phase noise (AM-PM) conversion must be judiciously avoided.

2.1.9 Recording equipment

The first observations appearing in this work were made using Mark II system which utilised standard video cassettes. Mk II could record a 2 MHz bandwidth and the cassettes had to be changed every two hours.
A considerable increase of performance especially in the recording bandwidth which translates directly to sensitivity was achieved with the Mk III system that was designed around a Honeywell 96 tape reel recorder. European Penny&Giles produced a number of tape transports mainly for use in the JIVE correlator.
Another track of evolution was the Canadian S2 system that used multiple video recorders to achieve higher bandwidth and the Japanese system which utilises a HDTV-cassette recorder and is capable to record 1024 Mbit/s (Giga-bit Recorder GBR-1000). A detailed review of VLBI recording technology is found in Rogers (1991) and Kellermann & Moran (2001).
The future media for VLBI data will probably be the standard computer hard disks that are specially packaged to tolerate transportation. For pre-session performance tests and also for observations requiring smaller bandwidth fast Internet connections can and have already been used.

2.2 Imaging

2.2.1 Deconvolution

Because the UV-plane is very sparsely sampled, direct evaluation of Eq. 2.9 produces a number of artifacts, which can totally hide the true structure of the source and in any case limit the dynamic range.
Fortunately there is additional information that can be used to patch the voids, e.g., *positivity of the true brightness distribution, finite source size, smoothness of the sky* and that *the sources can be represented by a small number of point sources.* The deconvolution algorithm should use this extra information to interpolate the visibilities and solve Eq. 2.9 for a most plausible brightness distribution.
Currently the most popular deconvolution algorithm for radio interferometry is CLEAN. It was invented in early 70's by Jan Högbom while he was working on the design of the Westerbork array (Högbom 1974).
CLEAN starts by locating the largest value in the dirty image (Eq. 2.9). It then subtracts a downscaled (usually a few percents of the peak) copy of the dirty beam (Eq. 2.8 centered to the peak and adds a corresponding delta function to the cleaned image. This is repeated until a selected criterion has been fulfilled (first negative delta-component, number of iterations, adequate residual noise level). The cleaned image, which now contains a collection of delta-functions is then convolved with a suitable *restoring beam*, which is usually a Gaussian with the same half-power width as the dirty beam. The residual emission is finally added to the cleaned image to give an indication of the real noise level of the image.

It can be tempting to use a considerably smaller or a circular restoring beam to achieve super-resolution in one or both beam axes. This usually does not produce very good results because the Fast Fourier Transform (FFT) algorithm that is generally used to calculate the dirty beam and -image does not behave very well in the presence of noise and corrupts the derivatives of the visibilities which are the basis of super-resolution. In other words, a smaller restoring beam brings potentially erroneous extrapolated information outside of the UV-plane to the image. Conversely, interpolation fidelity can be improved by using a larger restoring beam (Briggs 1995).

A number of variants have been developed based on the the classical Högbom CLEAN algorithm. Information on the finite source extent can be brought into the algorithm by allowing the algorithm to subtract components only within limited regions (CLEAN boxes).

Another popular deconvolution method used for VLBI images is the maximum entropy method, MEM (Cornwell & Evans 1985). There are numerous interpretations of the justification of this method but the consensus is that at least it minimises the variance of the pixel values and keeps the image positive. In addition to minimising the χ^2 of the model and the data, the algorithm maximises $\mathcal{H}$:

$$\mathcal{H} = -\sum_k I_k \ln \frac{I_k}{M_k e}, \tag{2.26}$$

where I_k is the intensity of the pixel k in the image I. M_k is a *default image* which can simply be a flat field with an approximate total flux of the source or a low resolution image.

MEM is good with diffuse emission and somewhat faster than CLEAN on large fields, but has difficulties in removing sidelobes when a point source is on top of a resolved emission. For these reasons, CLEAN is often preferred over MEM in high frequency compact source imaging.

Deconvolution can correct only the effects of discrete sampling because the dirty beam or PSF is assumed to be accurate. Time dependent phase and amplitude errors change the PSF continuously and without yet another extra trick VLBI imaging would be impossible.

2.2.2 Closure quantities

In the early 1950's Roger Jennison, when trying to measure fine structure of radio sources, discovered that when the phases of three baselines are summed up, all the antenna based phase errors are cancelled (Jennison 1958). This can be easily seen by calling the visibility phases of antennas i, j and k as ϕ_{ij}, ϕ_{jk} and ϕ_{ki} and the antenna based phase errors as θ_i, θ_j and θ_k. The *closure phase* C_{ijk} is then

$$\begin{aligned} C_{ijk} &= \phi_{ij} + \theta_i - \theta_j \\ &+ \phi_{jk} + \theta_j - \theta_k \\ &+ \phi_{ki} + \theta_k - \theta_i \\ &+ \epsilon \\ &= \phi_{ij} + \phi_{jk} + \phi_{ki} + \epsilon, \end{aligned} \tag{2.27}$$

where ϵ denotes the thermal noise component. The negative sign of the second antenna based phase arises from the complex conjugate in the definition of visibility (e.g. Eq. 2.2). Closure amplitude Γ_{ijk} can be defined in a similar way for visibility amplitudes A and (amplitude) gain errors g:

$$\begin{aligned} \Gamma_{ijk} &= \frac{g_i g_j A_{ij} \cdot g_k g_l A_{kl}}{g_i g_k A_{ik} \cdot g_j g_l A_{jl}} \\ &= \frac{A_{ij} \cdot A_{kl}}{A_{ik} \cdot A_{jl}}, \end{aligned} \tag{2.28}$$

so a closed loop of four baselines is needed to calculate the closure amplitude.
All errors do not close, in fact all errors that are related to the baselines, e.g. bandpass differences between stations and problems in station data acquisition electronics. Closure errors rarely exceed thermal noise in high frequency AGN observations. If in doubt, bandpasses can be calibrated and the station electronics are not likely to be a problem because network performance is continuously monitored.
In any case non-closing errors are dangerous because they violate the assumptions that make the modern VLBI imaging possible.

2.2.3 Hybrid mapping and self calibration

Unfortunately, the closure quantities cannot be used to produce images directly. Therefore, they are usually incorporated in the deconvolution process.
Early methods, variants of the *hybrid mapping algorithm*, resemble the Gerchberg-Saxton phase retrieval algorithm that is used in electron microscopy and subsequently in antenna surface holography (Gerchberg & Saxton 1972). Hybrid mapping starts with a trial map which is Fourier transformed to trial visibilities. Some of the visibilities can be computed from the closure phases and are used instead of the trial visibilities (Readhead & Wilkinson 1978). After this the modified trial visibilities are inverse transformed to produce the hybrid map. Another variant adjusts the unknown errors so that the difference between hybrid and trial maps is minimised (Cotton 1979). The resulting hybrid map is usually CLEANed with constraints and it forms the trial map for the next iteration. When calculating the phases explicitly the error distribution of the phases is non-Gaussian. Errors and difficulties arise in subsequent processing since e.g. least squares algorithms assume

Gaussian distribution. Also incorporating antenna based a priori information, e.g. atmospheric phase changes (Eq. 2.21), is difficult.
If a process alters only the complex gains of the antennas and visibilities are not corrected directly, it automatically conserves the closure phases. Changing only antenna gains is also more natural since most of the errors are antenna based and handling non-Gaussian error distributions can be avoided.
The corrections g_i and g_j to the gains can be found by using *self-calibration* (Cornwell 1998 and references therein), i.e. by minimising

$$S = \sum_k \sum_{\substack{i,j \\ i \neq j}} w_{ij}(t_k) \left| V_{ij}^{\mathrm{obs}}(t_k) - g_i(t_k) g_j^*(t_k) V_{ij}^{\mathrm{model}} \right|^2 , \tag{2.29}$$

where $w_{ij}(t_k)$ is a weight depending on the variance of the visibility, V_{ij}^{obs} and V_{ij}^{model} are the observed and model visibilities. Usually only the gains are modified using Eq. 2.29, the model is adjusted in an outer loop by a deconvolution algorithm, typically CLEAN, MEM or model fitting (Section 2.2.4).
The timespan over which the gains, especially the amplitude part, are held constant depends on SNR, atmospheric coherence time and also the source structure. If the gains are allowed to change too freely, some features from the erroneous model can be get 'freezed' to the gains and prevent convergence in the outer loop. It is also detrimental to use too many free parameters in the model: if an erroneous model can explain the observed visibilities exactly, the gain adjustments resulting from Eq. 2.29 are obviously $g_i = g_j \equiv 1$ and convergence is halted.

2.2.4 Model fitting

It is often advantageous to operate in the UV-plane and examine the visibilities directly. This is especially true when the quality of the visibility data is poor: SNR is low and/or UV-coverage is sparse, i.e. typical situation in global high-frequency VLBI. Unless the source is very simple (single or double Gaussian), fitting the visibilities to a model and examining the residuals is easier.
If the source is simple enough, i.e. can be described using with a number of Gaussians or other simple functions, model fitting is usually the best method to extract physical parameters from the data. Additionally the imaging algorithms that utilise self-calibration benefit from a better starting model if the source is considerably different from a point source, e.g. the source has two or more approximately equal components or is otherwise complex.
Generally speaking both CLEAN and MEM are also model fitting algorithms, CLEAN fits delta functions and MEM image patches or pixels to the visibility data. Therefore in comparison the model fitting algorithm has to cope with considerably fewer degrees of freedom in typical high frequency AGN images, and information is concentrated describing the few model parameters. Occam's Razor is in action if model fitting is used properly, i.e. starting with a point source model and adding parameters while self-calibrating

until the fit is not improved when adding components.
Of course model fitting has its limitations, imaging very complex diffuse sources is handled better with CLEAN and MEM. However, e.g. fitting out simple structures from image and letting the more complicated algorithms take care of the rest improves dynamic range and speeds up convergence. A model is good only if it describes not necessarily the source, but the observed true visibilities within the limits set by thermal noise.
Sometimes two models of a source are physically equally likely, e.g. a single component or two close components in the AGN core and furthermore both of the models fit to the visibilities equally well. If observations from a triangle of long baselines are available, the decision is easy to make: fit the data with both of the hypotheses and examine how the *closure phases* fit to the models. If there is no difference in the phases between the two models which is exceeding the noise level, a one-component model must be chosen (according to Occam's Razor). If there is a clear difference favouring a more complex structure, a splitted core model is justified (Paper [P6]).
Unfortunately the option to use closure phases in model fitting is not available in the current software packages. In many cases, like when producing a starting model for subsequent self-calibration loop, closure phase fitting would be a very robust method because it is totally insensitive of any calibration errors. The reason why closure quantities are not utilised is probably because the error distributions are non-Gaussian and so the conventional least squares algorithms are not valid.
Unlike with the imaging algorithms, it is possible to estimate errors in extracted parameters when model fitting is used. Traditionally this has been done by calculating the the χ^2 covariance matrix. The diagonal of this matrix gives formal errors of the fit but does not take into account that the antenna gains are not necessarily correct and can be adjusted to support a slightly different model. Combined with ignored correlation between the parameters results in overoptimistic error estimates.
One attempt to tackle this problem is to change the parameter in question in discrete steps while allowing other parameters to adjust to the change while performing a self-calibration in each step. The range of a 'good fit' is determined visually from the fitting residuals. This approach adopted by Difwrap (Lovell 2000 and references therein) generates usually somewhat pessimistic error estimates when compared, e.g., to the quality of closure phases, and relies on the subjective judgement.
The lack of robust fitting and error estimation method is unfortunate since model fitting could clearly provide much more accuracy in determining component positions and brightness temperatures than the formal beamsize of the array.
Fig. 2.2 shows why phase information is crucial in interferometry. While amplitudes are nearly identical, a look to the phases reveals immediately the true nature of the source.

2.3 High resolution VLBI

There is basically only one way of improving the resolution in VLBI: increasing the baseline length in wavelengths. This can be done by increasing the physical length of the baseline e.g. by using an orbiting telescope, (Fig. 2.3, HALCA satellite in the VSOP

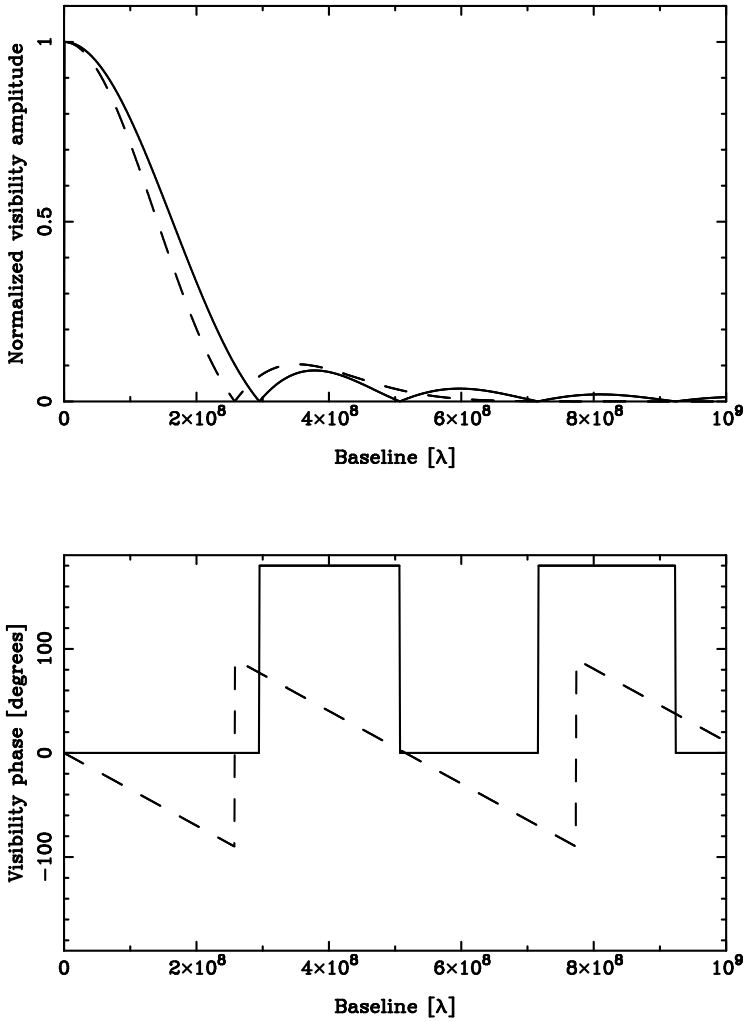

Figure 2.2: The visibility amplitudes and phases of two different source models: solid lines represent an optically thin sphere with a radius of one milliarcsecond and dashed lines a Gaussian double source with both radius and separation of 0.4 milliarcseconds.

project, Hirabayashi et al. (1998)) or by decreasing the observed wavelength (Paper [P5]).

Both approaches have their merits: some phenomena, like molecular spectral lines can be observed only at distinct frequencies. In some cases, like when observing the cores of AGN, a sufficiently high frequency should be used to reach the optically thin part of

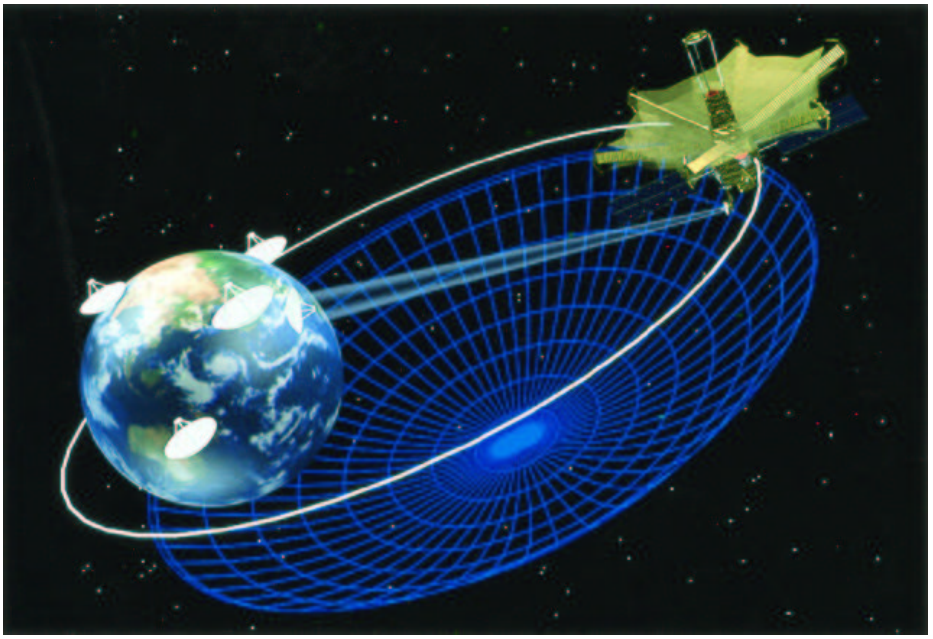

Figure 2.3: For ground-based VLBI experiments, the longest projected baselines are limited to 10,000 km. When using an orbiting telescope, this constraint can be avoided. In the case of HALCA, the total array size is up to three times larger than the longest earth-based baseline (Hirabayashi et al. 1998).

the spectrum to be able to really see deep to to the core. In most cases these approaches should be combined to get comparable resolution in both regimes to get reliable information both from the spectrum and the structure of the source.
Currently the state-of-the-art in ground-based VLBI are the ongoing 2 mm (147 GHz) global experiments (Paper [P5] and Fig. 2.4). In the near future, ground-based 2 mm VLBI will probably become a routine and experiments will move to 1.3 mm.
HALCA spacecraft has been observing routinely at 6 and 18 cm from 1997. VSOP-2, the successor of HALCA which is currently in planning stage, will be pushing the limits in resolution (25 μas), sensitivity (60 μJy/beam) and observing wavelength (6 cm – 7 mm).

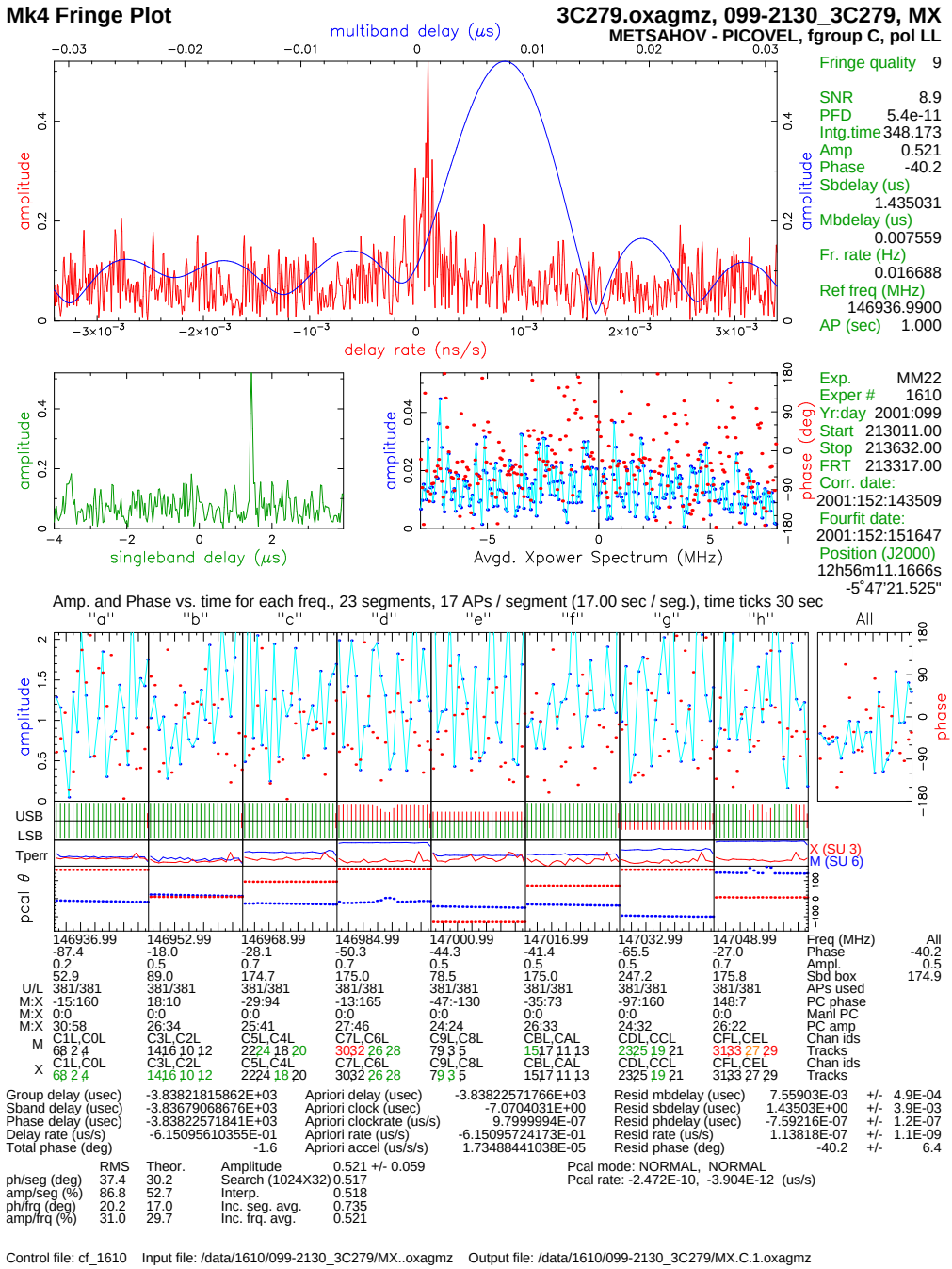

Figure 2.4: A MK4 correlator (Max Planck Institut für Radioastronomie) fringe plot of the Apr 9 2001 experiment between Pico Veleta (Spain) and Metsähovi (Finland) telescopes. The strong correlation peaks in the multi- and singleband delays and in delay rate are the signs of a successful experiment.

CHAPTER 3
Active Galactic Nuclei

Active Galactic Nuclei (AGN) form a peculiar and much studied group of extragalactic objects. They are the most luminous objects known, with variability timescales from years to hours. This leads to serious problems if one tries to explain the energy production using stellar processes. Even if the shortest timescales are currently believed to be caused by interstellar scintillation, a much more efficient energy production method than stellar processes is needed. In addition, AGN radiate over the whole spectrum from radio frequencies to gamma-rays. The AGN can be divided in two groups according to their emission in radio frequencies. The radio loud AGN produce highly collimated jets of relativistic energetic particles. The jets radiate synchrotron emission and form extended radio lobes at their ends that are especially well seen at low radio frequencies. The radio quiet AGN do not have (detectable) jets but are yet not totally quiet at radio frequencies.

3.1 Basic Model

The current standard model to explain the observed properties consists of a supermassive black hole and a surrounding accretion disk where the matter circulates before it falls to the black hole (Fig. 3.1). The accretion disk consists of hot optically thick plasma and it is glowing brightly in ultraviolet (UV) and possibly in soft X-rays. The innermost region of the accretion disk contains hot optically thin plasma and generates medium and hard X-ray emission.
In some AGN clumps of line emitting clouds move around the core region at high velocities. This region emits very broad spectral lines from UV to near infrared and is called the broad line region (BLR). It surrounds the central engine up to about 1 parsec (pc).
The central region is surrounded by a warped disk or a torus of dust. The torus obstructs the view to the central engine except when viewed along near the axis. This viewing angle dependency leads to the unification models.
In the outermost shell a cooler region that emits narrow spectral lines (NLR) extends up to some hundred pc.

3.2 Jets

The collimated jets are responsible for most of the radio emission from AGN. They carry energy from the central engine to distances of several kiloparsecs. The jets themselves are mostly invisible in high frequency VLBI images, and the prominent features are the shocks that travel along the jet.

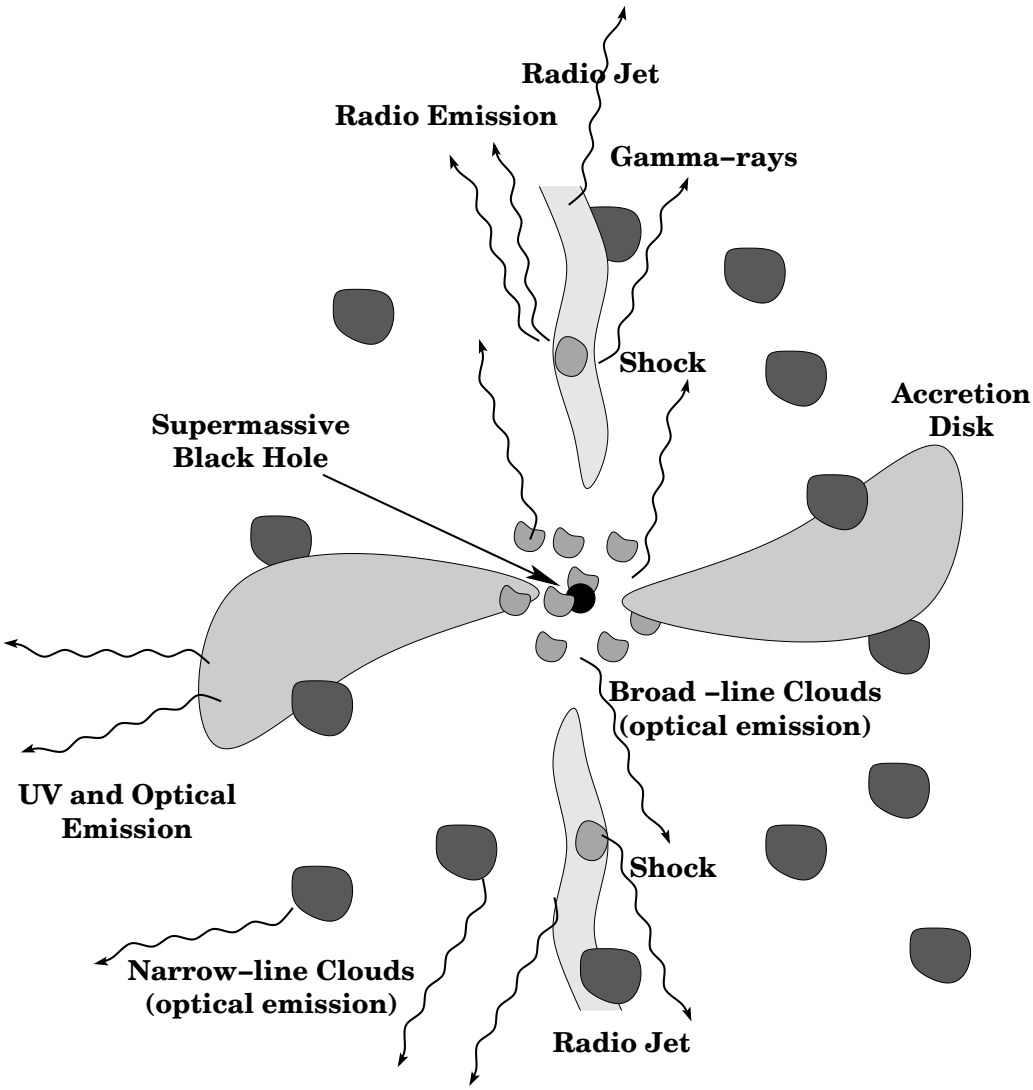

Figure 3.1: A schematic representation of a generic nucleus of an active galaxy. An accretion disk surrounds a supermassive black hole, radio emission and gamma-rays are produced mainly in the jets which are perpendicular to the accretion disk (not to scale).

The energy that creates the shocks and the jet travels through an invisible funnel to the VLBI core, which is located at the apex of the radio jet (Fig. 3.2) .

An intriguing question is what happens when an instability from the central engine is arriving from the funnel to the VLBI core; is it just becoming visible in radio and starts its travel along the jet, does it create a standing shock and make the core brighten (a core

flare) or does the instability hit the core and generate only a very weak shock in the jet but a considerable brightening of the core.
The jet can also bend, sometimes quite abruptly to 90°. This has been explained either by a cloud of interstellar medium to which the jet is colliding or by helicity of the jet (Paper [P7]).

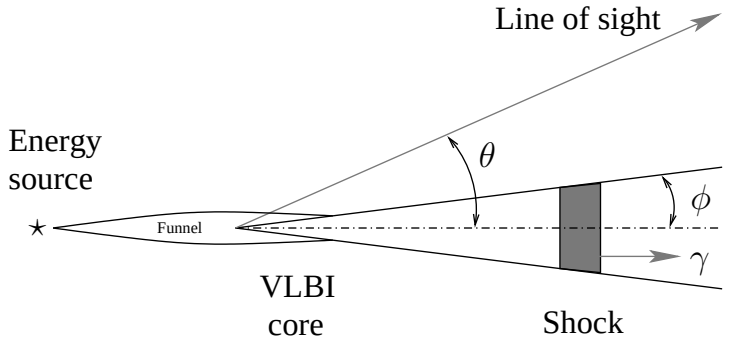

$$\Gamma \equiv \gamma = \frac{1}{\sqrt{1-\beta^2}} \qquad \beta = \frac{v}{c}$$

Figure 3.2: Schematic of a shock-in-the-jet-model. Energy is transmitted to the jet through an invisible funnel. A shock forms in the VLBI core and starts to move along the jet and expands adiabatically. θ is the viewing angle, ϕ is the opening angle of the jet and γ is the bulk Lorentz factor of the flow.

CHAPTER 4
Total flux density variations and VLBI

Perhaps somewhat surprisingly, the connection between radio flaring and the structure changes seen in VLBI images is not very well understood. It is generally accepted that the chain of events begins from some kind of a disturbance in the accretion disk, a quake or crossing of another accretion disk as proposed in the case of OJ287 (Takalo 1994, Sillanpää et al. 1996). This causes a change in the flow of the relativistic jet and a shock starts to travel along the jet. This shock is then seen in the VLBI images as a moving brightening which is also called a knot or a VLBI component.
The core can brighten without a detectable VLBI component ejection and it is clear that not all features seen in the VLBI jet can be assigned to a previous radio flare. Some components can be too weak or fade out before they can be resolved from the core, as in the case of 1749+096 (Paper [P3]) which has undergone a violent flaring without a noticeable ejection seen in the 22 GHz VLBI images. By inspecting carefully the closure phases at 22 GHz a second component very close to the core can be detected. This close component and also the jet direction was verified by 86 GHz VLBI observations (Lobanov et. al 2000).

4.1 Decompositions of total flux density time series

Although the flaring process is not understood to the extent that it could be physically modelled, it is possible to use a simple ad hoc model consisting of exponential rise, sharp peak and exponential decay (Valtaoja et al. 1999):

$$\Delta S_i(t) = \begin{cases} \Delta S_{\max,i}\, e^{(t-t_{\max,i})/\tau_i}, & t < t_{\max,i} \\ \Delta S_{\max,i}\, e^{(t_{\max,i}-t)/1.3\tau_i}, & t > t_{\max,i} \end{cases}, \tag{4.1}$$

where $\Delta S_{\max,i}$ is the maximum flux density of flare i, $t_{\max,i}$ is the epoch of the maximum and τ is the timescale of the flare. The total flux of the source at a given time is

$$S(t) = \sum_i \Delta S_i(t) + S_{\rm Q}, \tag{4.2}$$

where $S_{\rm Q}$ is the quiescent flux of the source.
The starting point of a flare, $t_{0,\rm TFD}$ (and therefore the ejection epoch of a new shock if a connection is found), has traditionally been defined as the nearest previous local minimum of the flare ($t_{\rm lm}$). This causes clearly bogus results if two flares occur nearly simultaneously because the local minimum occurs in this case between the maxima and

therefore very near the maximum epoch of the first flare. When utilising decomposition, the contribution from the individual flares can be separated and a per-flare criterion for the starting point can be defined.
The choice of $t_{0,\mathrm{TFD}} = t_{\max} - \tau$, which is identical to $S(t_{0,\mathrm{TFD}}) = S_{\max}/e$, may look arbitrary but if it is compared to t_{lm}, the average difference is zero with standard deviation of 0.4 years. So these two definitions are in practice identical except that $t_{0,\mathrm{TFD}}$ avoids the problem with local minima (which is the cause of high standard deviation).
This simple model allows us to identify the flares and extract parameters that characterise the flare from the unevenly and sometimes sparsely sampled total flux density (TFD) data.

4.2 Relativistic effects

When the speed of an emitting source is relativistic, the finite speed of light must be taken into account (e.g. Urry & Padovani 1995, and references therein). A convenient parameter describing the relationship between the source velocity $\beta = v/c$ and the viewing angle θ is the *Doppler factor* δ [1]:

$$\delta = \frac{1}{\gamma(1 - \beta\cos\theta)}, \tag{4.3}$$

where

$$\gamma = \frac{1}{\sqrt{1-\beta^2}}, \tag{4.4}$$

is the *Lorentz factor* of the source.
When the source is approaching the observer, it is catching up the photons it is emitting. This causes *time dilation*, i.e. the time intervals measured in the source rest frame are longer than in the observer frame:

$$t' = \delta t, \tag{4.5}$$

where t and t' are the times in the observer and source rest frames and primed quantities refer to the source rest frame. Because the number of wavefronts per unit time is constant, the emission is blue-shifted:

$$\nu' = \delta^{-1}\nu, \tag{4.6}$$

where ν and ν' are the frequencies in the observer and source rest frames respectively. The solid angle is transformed also:

$$\mathrm{d}\Omega' = \delta^{-2}\mathrm{d}\Omega. \tag{4.7}$$

Doppler boosting in intensity is defined by

$$I_\nu(\nu) = \delta^3 I'_{\nu'}(\nu'), \tag{4.8}$$

[1] There are two conventions in the literature: $\delta \equiv D$ and $\gamma \equiv \Gamma$.

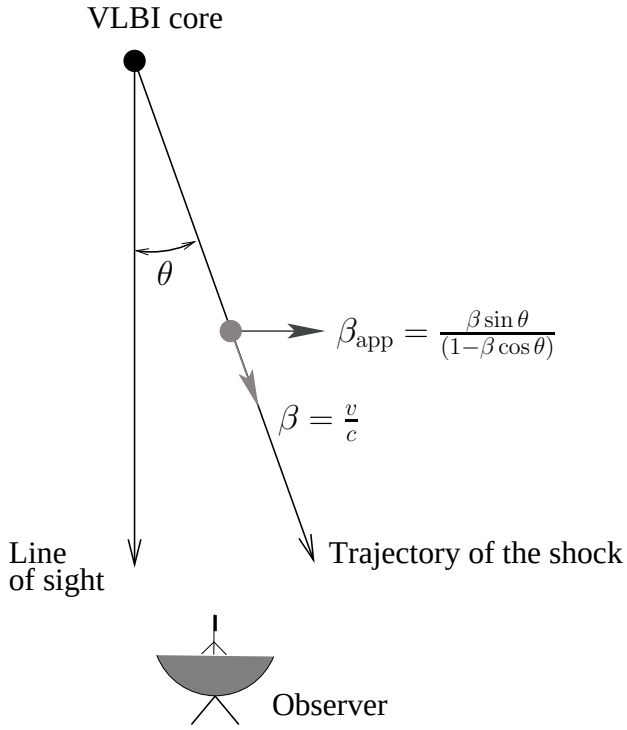

Figure 4.1: When a shock is travelling nearly towards the observer at angle θ at relativistic speed v, the apparent speed $\beta_{\rm app}$ can exceed the speed of light.

i.e. the intensity is enhanced dramatically. One power of the boosting comes from Eq. 4.5 and two from Eq. 4.7.
If the emission is isotropic in the rest frame of the source, the flux is boosted by the same amount. The spectral shape of the emission,

$$F'_{\nu'}(\nu') \propto (\nu')^{-\alpha}, \tag{4.9}$$

where α is the *spectral index* of the emission, has to be taken into account. Because the ratio of the intrinsic fluxes in emitted and observed frequencies is δ^{α} the flux density is boosted as

$$F_{\nu}(\nu) = \delta^{3+\alpha} F'_{\nu'}(\nu). \tag{4.10}$$

Relativistic motion towards the observer can also create an illusion of *superluminal motion*, i.e the observed velocity can appear to exceed the speed of light (Fig. 4.1). It can be easily shown from the geometry and the finite speed of the light that the apparent velocity is:

$$\beta_{\rm app} = \frac{\beta \sin\theta}{1 - \beta\cos\theta}. \tag{4.11}$$

This effect is used to find limits to γ, δ and θ in Paper [P7] (see also Section 4.4).

4.3 Connections between radio flares and VLBI images

4.3.1 Emission from close to the core

In Paper [P6] the TFD variations and VLBI modelfits of a sample of 27 blazars[2] from Jorstad et al. (2001) were compared to find out how large fraction of moving VLBI components can be associated with TFD flares. Eq. 4.2 was used to characterise and isolate the contribution of individual flares, and the extracted parameters $t_{0,\mathrm{TFD}}$ and $\Delta S_{\max}$ were compared with the results from VLBI.
Convincingly for 28 out of the 29 superluminal ejections we have studied, a TFD flare occurs within 0.5 years. The exception to this rule is one component in 3C279, its VLBI ejection time is not very well determined which probably causes the deviation. Also there is a high correlation between the VLBI component and TFD decomposition fluxes.
We do not have enough VLBI data to investigate if the opposite is true, i.e. if a TFD flare *always* produces a travelling shock. This kind of study requires dense high frequency VLBI monitoring, which has only recently become feasible due to the upgrade of 8 VLBA antennas to fully support 3mm observations.

4.3.2 Core flares

In most cases when a new VLBI component can be resolved from the brightened core, the total flux is already going down. This naturally leads to the assumption that the ejecta are a result of changes in the radio core and so the core can also brighten by itself without ejecting a new VLBI component. In Paper [P6] we found 24 cases of core flares from our dataset, i.e. the VLBI core flux rose 30% and the difference was greater than the TFD noise level. In six cases there were not enough VLBI data to study the jet behaviour after the flare. In 11 of the remaining 18 cases a new component appeared in the jet. Also, the flux behaviour of this new component matched with the TFD flare.
This new evidence suggests that at least in some cases the core brightening is caused by a new component which is just blending with the core because of finite beamsize of the instrument and the actual core brightness remains constant. To investigate this further we searched suitable cases by calculating the assumed separations using expansion speed estimates from Jorstad et al. (2001). We found four cases where the separation was larger than one third of the formal beamsize of the array (0420-014, epochs June 21 and August 4 1995, 0528+134 Apr 22 1995, and 1156+295 May 4 1996). An associated epoch where the estimated separation was smaller than our criterion was (fortunately) also taken to the closer study (0420-014 April 22 1995). We also selected a control epoch so that there should be no components near the core i.e. the VLBI observation was well before the next flare and well after the previous one.
The published modelfits of these cases did not contain any close components. This is expected because this extra component has a noticeable effect only to the visibilities of the few long baselines. Consequently by adding this close component to the model

[2] A subclass of AGN consisting of radio loud, highly polarised quasars and BL Lacertae objects.

improves the reduced χ^2 of the fit only marginally because the change is downweighted by the numerous shorter baselines where the effect is negligible.

This was clearly seen when we plotted χ^2 vs. core separation of the new component: there was clear but not very deep minimum around the estimated 'true' position of the component. The statistical significance of this minimum is very difficult to determine because the complex gains of the antennas are not independent due to the use of selfcalibration and especially bad amplitude calibration can produce even a false local minimum.

In this case, when the sources are reasonably simple, it is possible to get information on the fine structure of the core by looking at the closure phases (see Section 2.2.2) of the triangles consisting of long baselines, in this case triangles including both Mauna Kea and Saint Croix antennas. It is immediately seen that the closure phase is not zero, which is a clear sign of compact structure.

However, the compactness can be anywhere in the source, two close components downstream of the jet could also produce non-zero closure phases.

Unfortunately, the current software packages that are used to reduce VLBI data are not using closure phases directly in model fitting. Instead, they are relying solely on selfcalibration, which is considered to be superior to the direct use of closure quantities. In general this is true but especially when analysing high frequency VLBI data of simple, compact sources, direct inspection of closure phases can prove to be very useful.

We fitted two models to the data: the first is basically the published model which does not contain compactness near the core but otherwise represents best fit to the data. The second is produced from the first by splitting the core into two close components (with the core flux divided between the two components). Usually a phase selfcalibration assisted the model to converge and a good fit also to the closure phases was achieved. In some cases an additional amplitude selfcalibration was necessary to improve closure phase convergence.

The results that are shown in Figs. 4.2 and 4.3 are encouraging: in all cases the second, 'double core' model, which is plotted in solid line, is better. The difference is striking in triangles consisting of long baselines. Even the first epoch of 0420-014 (April 1995), where the shock is very close to the core shows a slightly better fit.

It is possible that when moving through the core region, the disturbance both brightens the core *and* causes a shock in the jet. There is some evidence to support this because in some causes the shock is seen already when the flare is peaking, and therefore the flux of the core is not constant. Unfortunately, when trying to resolve this by modelling the closure phases it is readily noticed that the flux ratio and the separation of the core and the ejected shock are somewhat interdependent. In other words, nearly the same closure phases are observed either when the core is brighter and the shock is farther away from the core, or when the fluxes are equal and the separation is smaller. A full correlation analysis of the parameters would give some probabilities between the cases of constant and changing core flux.

The main result is that a large fraction of the TFD flares that were studied in more detail could be associated with a VLBI component in the jet. Therefore it is likely that most of the flares, perhaps all, produce moving shocks which, in the case of core flares, just fade

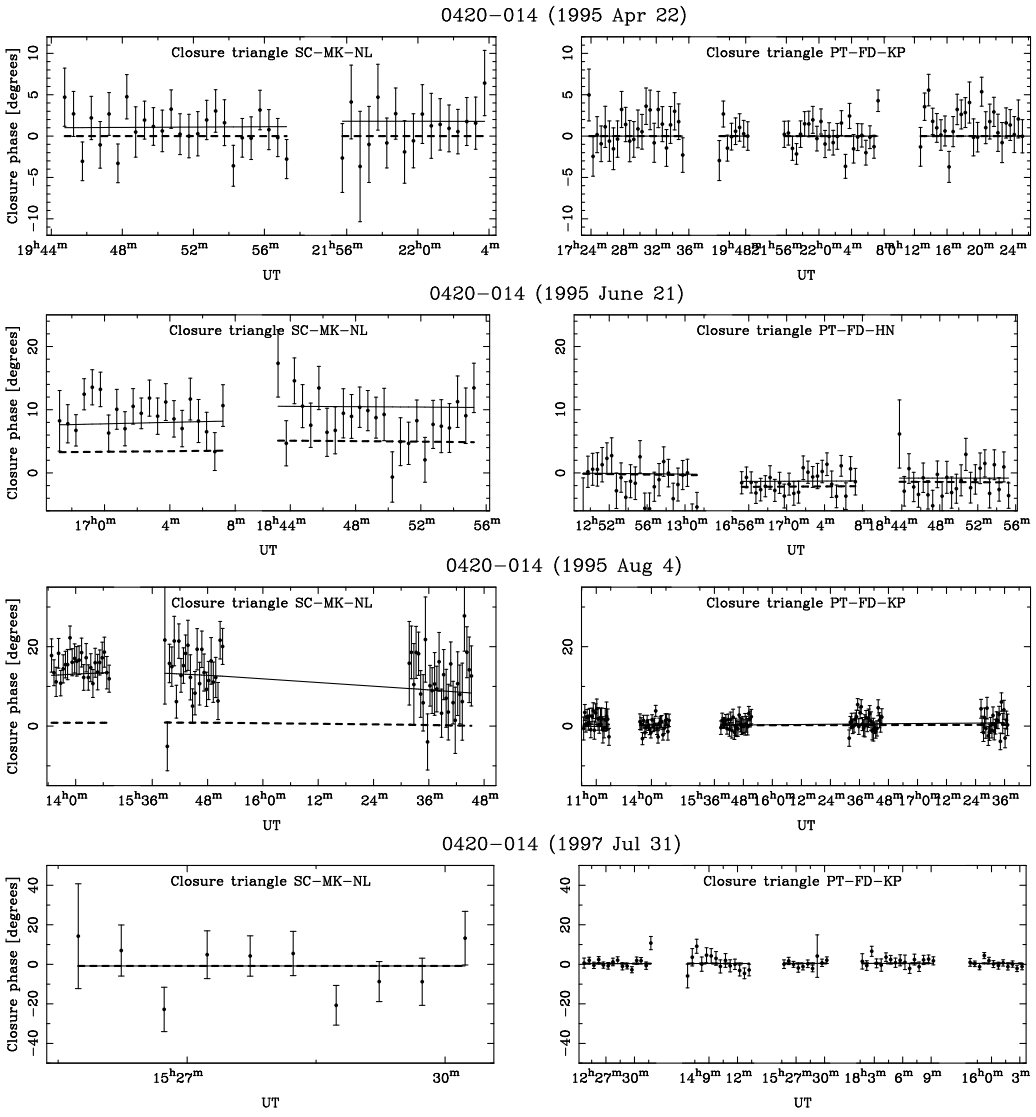

Figure 4.2: Closure phases from triangles consisting of long (left panels) and short (right panels) baselines from a series of observations of 0420-014. Two models are superimposed: one, perhaps an extended component in the core region (dashed line) and two components in the core region (solid line). The fourth epoch (August 4 1997) is for comparison: no close component to the core is expected nor found.

too much to be detected before they can be (easily) resolved from the core.
To be able to study the actual shock formation, dense (weekly) 3mm VLBI observations with one or two space baselines are needed. This requirement might be fulfilled within

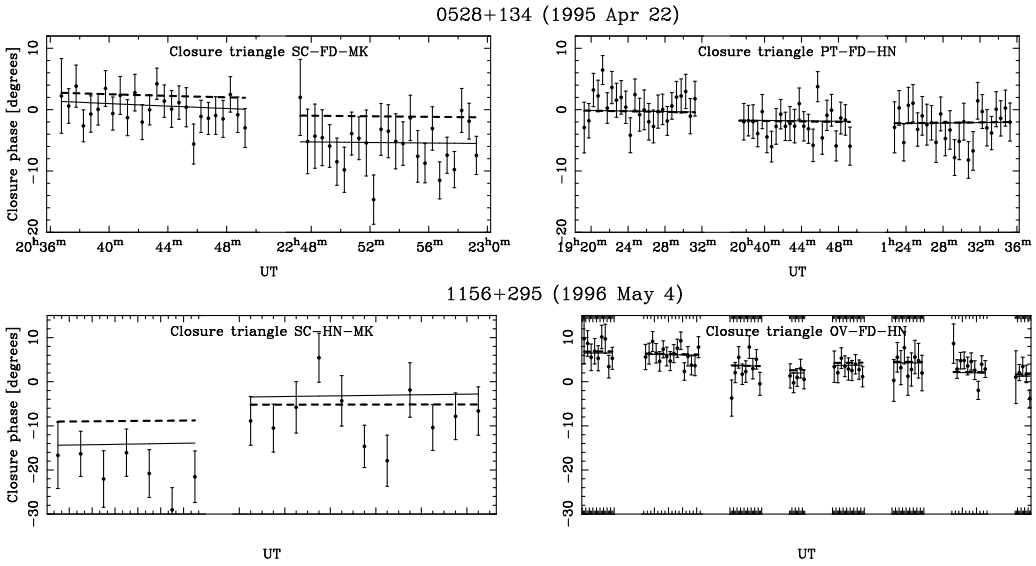

Figure 4.3: Closure phases from observations of 0528+134 and 1156+295. See previous figure for further description.

five years if the plans of VSOP-2 and/or iARISE proceed as expected.

4.3.3 The gamma-ray connection

The result of the previous section implies that the shocks are the origin of the flux density variations from radio to at least infrared. This has important implications to the models trying to explain the gamma-ray production in AGN (Paper [P4]).

In Hartman et al. (2001) the state of the art model (Böttcher & Bloom 2000) is used to fit eleven radio to gamma-ray spectra. The model calculates both the direct jet synchrotron component and the inverse Compton components which consist of the synchrotron self-Compton (SSC) part with synchrotron seed photons and of the external Compton (EC) portion with accretion disk and/or BLR seed photons. The bulk Lorentz factor and electron energy distribution are varied to find a fit to the optical-to-gamma-ray spectra.

Although quite good fits are found, the basic assumption that the jet flow is the origin of the flux variations is flawed. Additional evidence towards our interpretation can be found by deriving the spectral shapes of the quiescent jet and shocks of 3C 279 and comparing them to the jet model given in Hartman et al. (2001) (Paper [P4]). It is clear that shocks must dominate the gamma-ray production.

The timescales of the gamma-ray outbursts are of the order of about a week. If the origin of the outbursts is in the changes of the physical parameters of the jet itself, problems arise because there is no known mechanism that is able to change the Lorentz factor of the bulk flow at this rate.

On the other hand, when the variability timescale of the shocks is extrapolated to 10 THz, which is the frequency of the gamma-ray seed photons, a more fitting timescale of a week is obtained.
EC models which propose that the seed photons come either from the accretion disk or are reflected from the broad line region are also suspect because according to the results of Papers [P6] and [P4] the gamma-rays are coming very far from these regions. The average EGRET [3] flare occurs two months after the formation of the shock, and in this time the shock has travelled a distance of 1.5 pc down the jet.

4.4 Curvature of the jet and stationary features

In some sources the ejected shocks do not follow a straight trajectory, but instead the path starts to wiggle and can even turn abruptly 90 degrees from the mean jet axis. It is fairly easy to explain these changes if the jet is following a helical path. As it is required for these sources that the jet must be relativistic and that the viewing angle must be small, projection effects have a significant effect in the apparent trajectory.
In Paper [P7] we present 22, 43, and 86 GHz VLBI observations of CTA 102, which exhibit all signs of a helical jet. Combining our observations and earlier data found from the literature (Wehrle & Cohen 1989, Rantakyrö et al. 1996), we can study changes in the proper motion of the components.

4.4.1 Viewing angle along the jet

The equations in Section 4.2 can be utilised to estimate the undulating viewing angles along a helical jet. Because we know only the apparent proper motion of the shocks $\beta_{\rm app}$, and not the true bulk velocity of the flow, we must make the following assumptions:

1. The bulk Lorentz factor γ does not change in time or over the observed distance.
2. The largest inferred $\gamma_{\rm min}$ from close to the core represents the γ of the components in the jet.
3. The proper motion $\beta_{\rm app}$ of the components does not change significantly over the range where the linear fit is done.

To estimate the viewing angles from $\beta_{\rm app}$, we can first assume that the viewing angle is optimum, i.e it gives the largest $\beta_{\rm app}$ and thus the smallest γ. The maximum value of $\beta_{\rm app}$ occurs when the viewing angle θ is

$$\theta_{\rm opt} = \arccos(\beta) = \arctan(1/\beta_{\rm app}). \tag{4.12}$$

Furthermore, when $\theta = \theta_{\rm opt}$,

$$\delta_{\rm min} = \gamma_{\rm min}, \tag{4.13}$$

[3] Energetic Gamma Ray Experiment Telescope on the NASA Compton Observatory (20 MeV – 30 GeV).

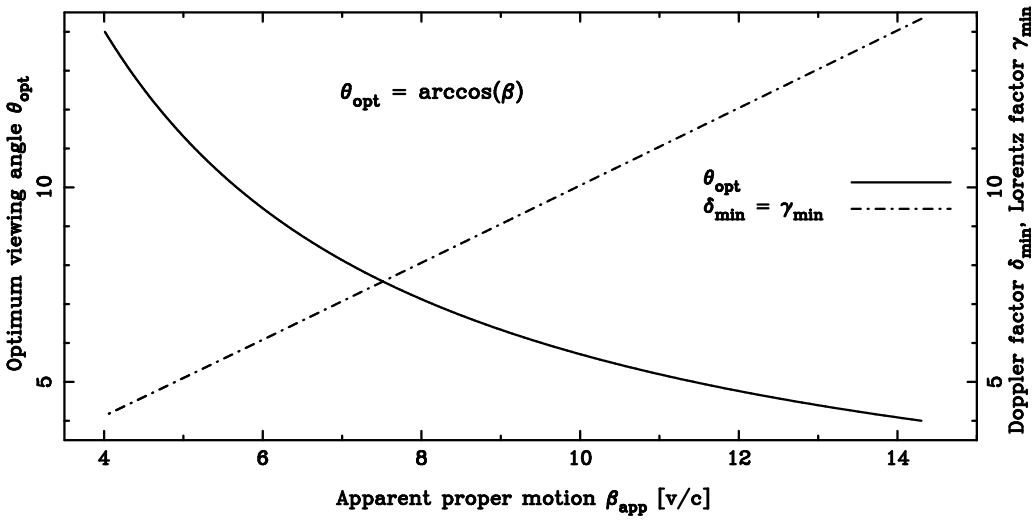

Figure 4.4: Optimum viewing angle and the minimum values of Doppler and Lorentz factors as a function of the apparent superluminal proper motion $\beta_{\rm app}$.

and additionally, when $v \sim c$

$$\beta_{\rm app} = \delta_{\rm min}\beta = \gamma_{\rm min}\beta = \sqrt{{\gamma_{\rm min}}^2 - 1} \simeq \gamma_{\rm min} \simeq \delta_{\rm min}. \tag{4.14}$$

In Fig. 4.4, $\theta_{\rm opt}$ is shown with the minimum Doppler and Lorentz factors $\delta_{\rm min}$ and $\gamma_{\rm min}$ as a function of the apparent proper motion.

4.4.2 Helical structure of the jet

The maximum value of the calculated lower limits is chosen to represent the constant Lorentz factor of the bulk flow in the jet. This choice is not a strong assumption since the variation of $\gamma_{\rm min}$ is quite small near the core and does not have a strong effect on the final conclusions.
Inverting Eq. 4.11 and using $\beta_{\rm app}$ of the shocks we can finally calculate the viewing angle estimates for the shocks (Fig. 4.5) moving at different core separations. The signature of a helical motion can be readily seen. Furthermore the standing features in the jet at 2 and 6 mas could be interpreted as Doppler enhancements of the underlying jet itself. It is also possible that because the viewing angle is going through a minimum at these points, the passing shocks are brightening and generating only an illusion of a standing shock (Fig. 4.6).

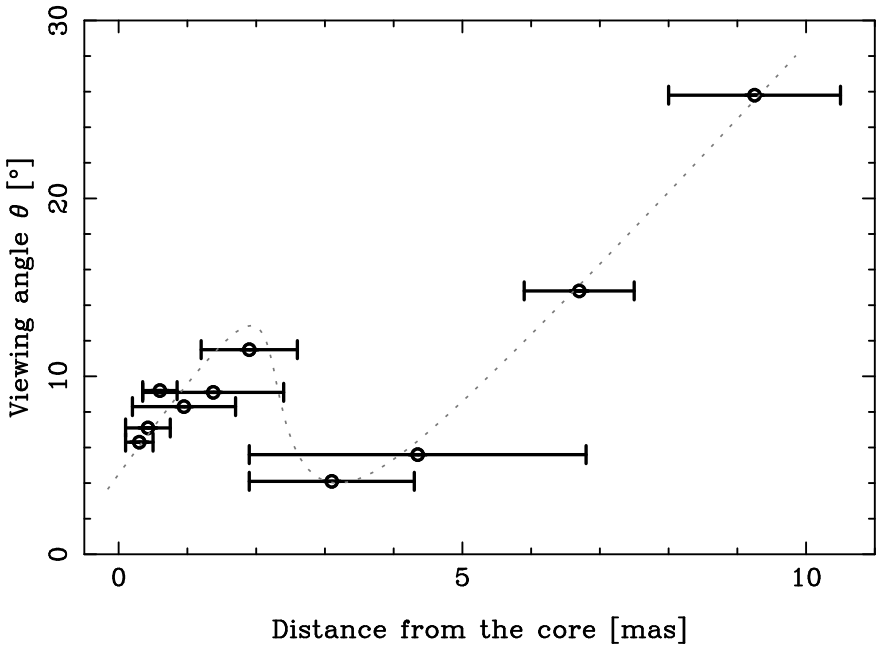

Figure 4.5: The inferred viewing angle as a function of separation from the core. The dotted line is not a fit to the points but rather an aid for the eye, representing a possible helical path of the jet.

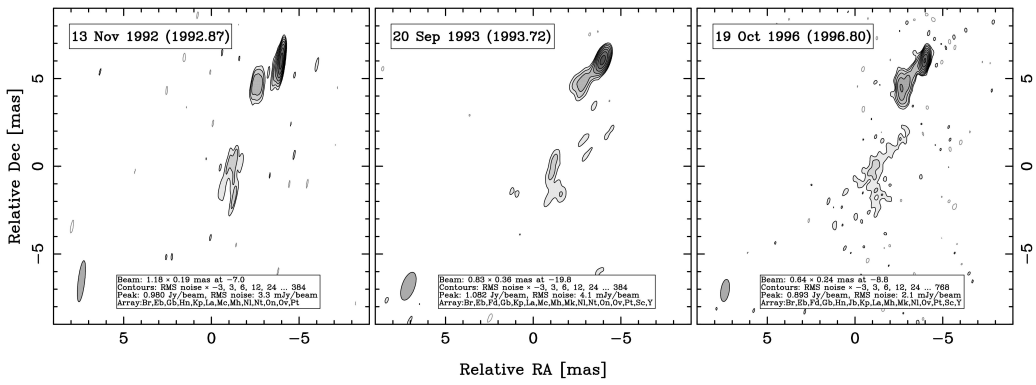

Figure 4.6: 22 GHz VLBI images of CTA 102. The standing features and helicity of the jet are clearly seen.

4.5 VLBI and cosmology

In principle, the geometry of the Universe can be determined by measuring the apparent size of a constant linear size object at different redshifts (z). In an Euclidean universe the angular size of such an object decreases in direct proportion to the distance. However, in four-dimensional cosmological models based on the Friedmann-Robertson-Walker geometry, the angular diameter (θ) may have a minimum near $z = 1$ and can increase at higher redshifts. The exact behaviour of the $\theta - z$ relation depends on the cosmological parameters, so it can therefore be used to determine the geometry of the universe (Fig. 4.7).

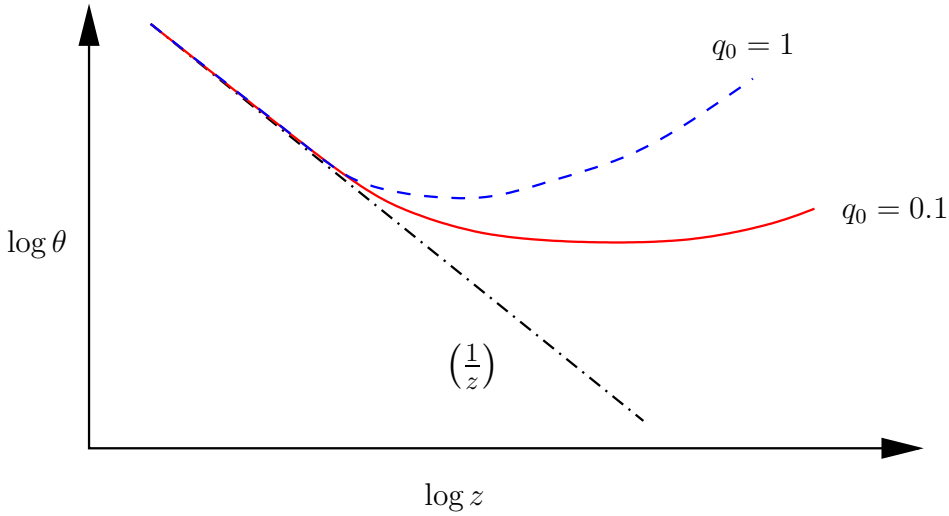

Figure 4.7: When an object of constant length is moved to cosmological distances, the angular size does not follow the monotonic 'common sense' $1/z$ relationship but instead has a minimum around $z = 1$ and starts to grow.

Unfortunately, there are severe difficulties in finding a good 'standard rod' which is not biased by cosmological epoch. All proposed objects such as galaxy clusters or double radio sources have similar diameters only on the average, and they evolve significantly with the cosmological epoch. In addition the results are confused by severe selection effects. In short, the problem with all proposed standard rods is that we cannot measure the true linear size of an individual object at cosmological distances. Instead of using the whole milliarcsecond structures as standard rods, we propose to use the sizes of the individual shocks propagating along the jets (Fig. 4.8, Paper [P2]).
As standard rods the VLBI shocks have several advantages over the previously used alternatives, although they do share many of the biases and selection effects. The shock size can be, and usually is, a function of frequency and therefore a function of redshift. The sizes can vary with cosmological epoch and physical environment of the AGN, and

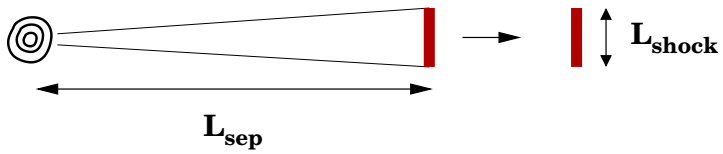

Figure 4.8: Instead of using the core separation distance $L_{\rm sep}$ as a standard rod, we propose to use the less biased and normalized shock size $L_{\rm shock}$.

are presumably dependent on the AGN luminosity. However, some other familiar sources of error and bias are absent.

The sources in a flux-limited sample are biased to have high Doppler boosting factors and thus small viewing angles. While this causes bias when using whole structures (Dabrowski et al. 1995) it works against the orientation bias when observing shock sizes. Because of relativistic aberration, the fast-moving shocks are always seen from the side. The quantity measured from the VLBI maps is therefore the transverse width of the shock. Furthermore, because the jet opening angles are small (Oppenheimer et al. 1994) the transverse size of an individual shock is nearly constant with time. The VLBI shock size may therefore be a better standard rod than the previously used total jet length. Large samples are still necessary for eliminating the various biases, selection effects and cosmological evolution.

However, the key advantage in using the shock sizes is that we thus have an independent method for estimating their true linear diameters. They are not just standard rods on the average; instead, each individual shock can be used as a calibrated rod.

A new shock becomes detectable both as an emerging VLBI component and as a flare in total flux density. Each flare has a characteristic variability timescale $\tau_{\rm obs}$ which can be estimated from flux monitoring data (Valtaoja et al. 1999). The transverse linear size L of the shock component is proportional to the light travel time across the emitting region filling the jet. We therefore have

$$L = K \cdot c \cdot \tau_{\rm int}, \tag{4.15}$$

where K is an unknown scaling factor that depends on the details of shock geometry and $\tau_{\rm int}$ is the true intrinsic variability timescale, corrected for redshift and Doppler boosting. One can further define the variability angular size as $\theta_{\rm var} = L/D_{\rm a}$, where $D_{\rm a}$ is the angular distance of the source. Since the derived $\theta_{\rm var}$ depends on the geometry of the Universe while the directly observable $\theta_{\rm VLBI}$ does not, a comparison of the two values for the same source can be used to reveal the geometry. This is the essence of our proposed new method: to use the relation $\theta_{\rm VLBI}/\tau_{\rm int}$ versus z.

In order to transfer the observed variability timescale $\tau_{\rm obs}$ into the source frame of reference $\tau_{\rm int}$, we must estimate the Doppler boosting factor δ of the source because

$$\tau_{\rm int} = \tau_{\rm obs} \left(\frac{\delta}{1+z} \right). \tag{4.16}$$

The traditional method for estimating the Doppler boosting factor is to use synchrotron-self-Compton arguments (e.g. Guerra & Daly 1997); however, such values are highly unreliable and much better ones can be derived simply by using total flux density variations (Lähteenmäki & Valtaoja 1999). Virtually all major total flux density outbursts in AGN have associated brightness temperatures (that are estimated from variability) far in excess of the equipartition limit $T_{\rm b,lim}$ (Readhead 1994; Paper [P1]), indicating significant Doppler boosting. The variability Doppler boosting $\delta_{\rm var}$ is given by

$$\delta_{\rm var} = \left(\frac{T_{\rm b,var}^{\rm source}}{T_{\rm b,lim}} \right)^{1/3}. \tag{4.17}$$

Unfortunately $T_{\rm b,var}^{\rm source}$ depends on $D_{\rm a}$ and z:

$$T_{\rm b,var}^{\rm source} \propto \theta_{\rm var}^{-2}(1+z)^3 \propto (1+z)^3 D_{\rm a}^2, \tag{4.18}$$

so we have to correct the original $\theta - z$ relation because the Doppler boosting factor derived from variability depends on the angular distance:

$$\delta_{\rm var} \propto D_{\rm a}^{2/3}(1+z). \tag{4.19}$$

The net result is that the 'normalized rod length' $\theta_{\rm VLBI}/\tau_{\rm int}$ has a weaker dependence on the angular distance, $D_{\rm a}^{-1/3}$ instead of the usual $\theta \propto D_{\rm a}^{-1}$.
By measuring both the angular and the linear sizes of our standard rods, we avoid most of the problems inherent in previous approaches. The main remaining source of uncertainty is the geometrical scaling factor K (Eq. 4.15), which plausibly could be dependent on source properties, for example if luminous AGN have different shock shapes than the weaker ones. The price to be paid is that we must be able to determine the Doppler boosting factors δ, and that the resulting $\theta_{\rm VLBI}/\tau_{\rm int}$ vs. z -dependence is weaker than in the usual case when variability Doppler boosting factors are used. This can be avoided if one uses boosting factors derived by other methods; however, such values tend to be so inaccurate that this method does not work any more (cf. Lähteenmäki & Valtaoja 1999). With constantly growing amounts of millimetre VLBI data becoming available, AGN shocks may prove to be the accurate and useful standard rods that were long sought after.

CHAPTER 5
Discussion of the papers

5.1 Three epoch survey of 15 AGN at 22 GHz

Paper [P3] VLBI monitoring of a sample of 15 AGN at 22 GHz. I. Data
Paper [P8] Comparison of Total Flux and VLBI Properties of a Sample of Fifteen AGN at 22 GHz
We have observed a sample of 15 bright active galactic nuclei (AGN) three times during 1992 – 1996 using the global 22 GHz VLBI network. The sample consists of all sources in the complete 2 Jy catalog of Valtaoja et al. (1992) that had not been observed at 22 GHz VLBI before our first epoch. Our aims were to obtain high-frequency and high resolution VLBI data on a representative sample of AGN. This data that consists of 45 VLBI images form the basis of the subsequent analysis and comparisons with TFD data, used in several other papers of this thesis. This project represents also the largest fraction of time that is spent for this thesis. In these papers we describe the observations and present images from the three epochs.

5.2 Comparison of VLBI and TFD data: new methods determining limiting brightness temperature $T_{\rm b,lim}$ and Doppler factor.

Paper [P1] Total flux density variations in extragalactic radio sources. II. Determining the limiting brightness temperature for synchrotron sources
Paper [P10] Comparison of Total Flux and VLBI Properties of a Sample of 15 AGN at 22 GHz
In these papers we present four new semi-independent methods determining Doppler boosting factor using TFD and VLBI data. We also present two new methods of estimating the limiting brightness temperature $T_{\rm b,lim}$ comparing Doppler boosting factors derived from TFD variability , radio and synchrotron-self-Compton fluxes and VLBI data. Both of these methods agree with the limit of $T_{\rm b,lim} \leq 10^{11}$K.

5.3 VLBI and cosmology

Paper [P2] The geometry of the universe from high resolution VLBI data of AGN shocks.
Paper [P9] AGN shocks as cosmological standard rods

In principle, the geometry of the Universe can be determined by measuring the apparent size of a constant linear size object at different redshifts. In an Euclidean universe the angular size of such an object decreases in direct proportion to the distance. However, in four-dimensional cosmological models based on the Friedmann-Robertson-Walker geometry, the angular diameter may have a minimum near $z = 1$ and can increase at higher redshifts. The exact behaviour of the $\theta - z$ relation depends on the cosmological parameters, so it can therefore be used to determine the geometry of the universe.
In these papers we propose to use the linear diameters of the shocks in AGN jets as standard rods for estimating the geometry of the Universe. The unique feature of shocks is that we can directly estimate their linear diameters from total flux density monitoring data and light travel time arguments. We demonstrate this method by using a small sample of 14 22 GHz VLBI observations. The accuracy of the derived values ($q_0 \simeq 0, \Omega_{\rm m} \simeq 0$) compares favourably with traditional methods using much larger samples.

5.4 Structure of the core region and the jet

Paper [P4] Millimeter continuum variations, VLBI structure, and gamma-rays: investigating shocked jet physics
Paper [P6] Connections Between Millimeter Continuum Variations and VLBI Structure in 27 AGN
Paper [P7] Multifrequency Interferometer and Radio Continuum Monitoring Observations of CTA 102
In these papers we compare the total flux density variations and the VLBI structural variations in a sample of blazars. We find that all the radio variations are due to shocks; the flux of the underlying jet remains constant. A large fraction of the shocks grow and fade within the innermost 0.1 mas, appearing only as 'core flares'. We show that most, if not all of the core brightenings are caused by the ejected shock that is within the synthesised beam of a mm-VLBI array. Comparisons with the EGRET data show that gamma-ray flares must come from the shocks, not from the jet. At the time of an EGRET flare, the shock is typically already over a parsec downstream from the radio core, beyond the accretion disk and/or the broad line region (BLR) photon fields. Thus, present models for gamma-ray production are inadequate, since they typically model the gamma-ray inverse Compton flux as coming from the jet, with significant disk or BLR external Compton components.
We show that the changes in proper motion of the shocks in the jet of CTA 102 are attributed to a change in the viewing angle of the jet rather than changes in the relativistic speed of the plasma.

5.5 2mm VLBI

Paper [P5] 147 GHz VLBI Observations: Detection of 3C 273 and 3C 279 on the 3 100 km Baseline Metsähovi – Pico Veleta

Very Long Baseline Interferometry observations at millimetre wavelengths (3 mm - 1 mm) provide the highest angular resolution and in self-absorbed quasars the possibility to explore their core regions and the origin of their jets.
While VLBI at 86 GHz (3.5 mm) on intercontinental baselines has become a routine observing facility (CMVA, VLBA), VLBI observations at even higher frequency are still in an experimental state.
In this paper we report on the first successful VLBI experiment at 147 GHz (2.1 mm) on the 3100 km long baseline (= 1.9 Mλ) between the 14-m telescope at Metsähovi (Finland) and the 30-m telescope at Pico Veleta (Spain). The sources 3C 273B and 3C 279 were detected with a SNR of $\sim$ 10.

Bibliography

Briggs, D. S. 1995, Ph. D. thesis, New Mexico Institute of Mining and Technology.

Böttcher, M., Bloom, S. D. 2000, AJ, 119, 469

Carilli, C. L., Carlstrom, J. E., Holdaway, M. A. 1998. ASP Conf. Ser. 180: Synthesis Imaging in Radio Astronomy II, 180, 565

Clark, B. G. 1998. ASP Conf. Ser. 180: Synthesis Imaging in Radio Astronomy II, 180, 1

Cornwell, T. 1998. ASP Conf. Ser. 180: Synthesis Imaging in Radio Astronomy II, 180, 187

Cornwell, T. J. , Evans, K. F. 1985, A&A, 143, 77

Cotton, W. D. 1979, AJ, 88, 1122

Dabrowski, Y., Lasenby, A., Saunders, R., 1995, MNRAS, 277, 753

Gerchberg, R. W., Saxton, W. O. 1972, Optik, 35, 237-246

Guerra, E.J., Daly, R.A., 1997, ApJ, 491, 483

Hartman, R. C., Böttcher, M., Aldering, G., et al. 2001, ApJ, 533, 683

Hirabayashi, H. et al. 1998, Science, 281, 1825

Hogg, D. C., Guiraud, F. O., Decker, M. T. 1981, A&A, 95, 304

Högbom, J. A. 1974, A&As, 15, 417

Jennison, R. C. 1958, MNRAS, 118, 276

Jorstad, S. G., Marscher, A. P., Mattox, J. R. et al. 2001, ApJS, 134, 181

Kellermann, K. I. , Moran, J. M. 2001, Ann. Rev. Astron. Astrophys., 39, 457

Leppänen, K. J. 1993, VLBA Scientific Memo No. 1.

Lobanov, A. P., Krichbaum, T. P., Graham, D. A. et al. 2000, A&A, 364, 391–408

Lovell, J. 2000, Astrophysical Phenomena Revealed by Space VLBI, Proceedings of the VSOP Symposium, Sagamihara, Japan, 2000, Eds.: H. Hirabayashi, P.G. Edwards, and D.W. Murphy, ISAS, p. 301-304., 301

Lähteenmäki, A., Valtaoja, E., 1999, ApJ, 521, 493

Napier, P. J. 1998. ASP Conf. Ser. 180: Synthesis Imaging in Radio Astronomy II, 180, 37

Oppenheimer, B.R., Biretta J.A., 1994, AJ, 107, 892

Pearson, T. J., Readhead, A. C. S. 1984, Ann. Rev. Astron. Astrophys. 22, 97

Rantakyrö, F. T., Bååth, L. B., Dallacasa, D., Jones, D.L, Wehrle, A. E. 1996, A&A, 310, 66

Rogers, A. E. E. 1991, ASP Conf. Ser. 19: IAU Colloq. 131: Radio Interferometry. Theory, Techniques, and Applications, 65

Readhead, A. C. S., Wilkinson, P. N. 1978, ApJ, 223:25

Readhead, A.C.S, 1994, ApJ, 426, 51

Shepherd M. C. 1997, ASP Conf. Ser. 125: Astronomical Data Analysis Software and Systems VI, 6, 77

Sillanpää A., Takalo L., Pursimo T., et al. 1996, A&A, 305, L17

Takalo, L. 1994, Vistas astron., 38, 77

Thompson, A. R., Moran, J. M., Swenson, G. W., Jr. 1986, Interferometry and Synthesis in Radio Astronomy, John Wiley & Sons, New York.

Urry, C. M., Padovani, P. 1995, PASP, 107, 803

Valtaoja, E., Lähteenmäki, A. Teräsranta, H. 1992, A&AS, 95, 73

Valtaoja E., Lähteenmäki A., Teräsranta H., et al. 1999, ApJS, 120, 95

Wehrle, A. E., Cohen, M. H. 1989, ApJ, 346, L69